Published in final edited form as:
Opt Express. 2009 April 27; 17(9): 7571–7585.

A three-dimensional multispectral fluorescence optical tomography imaging system for small animals based on a conical mirror design

Changqing Li[1], **Gregory S. Mitchell**[1], **Joyita Dutta**[2], **Sangtae Ahn**[2], **Richard M. Leahy**[2], and **Simon R. Cherry**[1]

Changqing Li: cqli@ucdavis.edu

[1] Department of Biomedical Engineering, UC Davis, Davis, CA 95616

[2] Department of Electrical Engineering, University of Southern California, Los Angeles, CA 90089

Abstract

We have developed a three dimensional (3D) multispectral fluorescence optical tomography small animal imaging system with an innovative geometry using a truncated conical mirror, allowing simultaneous viewing of the entire surface of the animal by an EMCCD camera. A conical mirror collects photons approximately three times more efficiently than a flat mirror. An x-y mirror scanning system makes it possible to scan a collimated excitation laser beam to any location on the mouse surface. A pattern of structured light incident on the small animal surface is used to extract the surface geometry for reconstruction. A finite element based algorithm is applied to model photon propagation in the turbid media and a preconditioned conjugate gradient (PCG) method is used to solve the large linear system matrix. The reconstruction algorithm and the system feasibility are evaluated by phantom experiments. These experiments show that multispectral measurements improve the spatial resolution of reconstructed images. Finally, an *in vivo* imaging study of a xenograft tumor in a mouse shows good correlation of the reconstructed image with the location of the fluorescence probe as determined by subsequent optical imaging of cryosections of the mouse.

1. Introduction

Three dimensional (3D) small-animal fluorescence optical tomography is an emerging tool to image non-invasively the distribution of fluorescence reporters and probes [1,2]. Fluorescence optical imaging of deep tissues is limited by the low spatial resolution due to photon scattering and low sensitivity due to photon absorption. Multispectral or hyperspectal measurements are a promising approach to improve the spatial resolution [3,4]. Compared with optical fiber-based fluorescence optical tomography systems [5,6], CCD based fluorescence optical tomography systems provide many more detector nodes, which potentially result in better spatial resolution [7]. So far, most CCD imaging systems have adopted a transmission mode in which the fluorescence measurements are taken at the opposite side of the illumination location [8–10]. In this paper, we present a prototype of a conical mirror-based 3D multispectral fluorescence optical tomography system for small animals in which the entire animal body surface can be observed simultaneously. This makes it possible to have more detector nodes for each illumination position. The system also is designed to permit multispectral detection. With this novel conical mirror, the CCD camera area is used more efficiently and more emission photons are detected compared with the use of multiple flat mirrors in a pyramidal configuration

OCIS codes: (110.6960) Tomography; (260.2510) Fluorescence; (170.3890) Medical optics instrumentation

– another geometry that allows visualization of the entire mouse surface [11]. A conical mirror approach for bioluminescence tomography imaging has also been proposed by others [12].

In this paper, we first describe the 3D fluorescence optical tomography imaging system in Section 2. In Section 3, phantom fabrication, mouse surface geometry extraction, 3D mesh generation and reconstruction methods are described. Imaging results, including an *in vivo* study, and discussion are presented in Section 4.

2. Experimental System

Fig. 1 shows a photograph and a schematic of the 3D fluorescence optical tomography imaging system. A 650 or 785 nm laser (BWF-OEM-650-200, B&W Tech Inc, Newark, DE for phantom experiments; BWF-OEM-785-1.0-100-0.2, B&W Tech Inc, for *in vivo* experiments) with a collimation lens at the end of its pigtail fiber is used to excite the fluorescence dye. A bandpass filter (650FS20-50, Andover Corporation, Salem, NH for phantom experiments; 780FS20-50, Andover Corporation, Salem, NH for *in vivo* experiments) placed in front of the laser rejects light at other wavelengths. Another lens focuses the beam into a small spot of ~1 mm diameter at the surface of the mouse. Two motorized scanning mirrors allow us to direct the laser beam (after reflection from the conical mirror) across the mouse surface. A transparent glass stage was placed in the center of the conical mirror to support the animal. Bandpass filters, placed inside a filter wheel, are used to select emission wavelengths. In the front of the filter wheel, an appropriate long pass filter (665FG07-50, Andover Corporation, Salem, NH for phantom experiments; LP02-785RU-25, Semrock Inc., Rochester, NY for *in vivo* experiments) is used to remove excitation laser spillover into the measurements at the emission wavelengths. An EMCCD (C9100-3, Hamamatsu Corp., Bridgewater, NJ) images the emitted photon distribution. Three line lasers, mounted on a linear stage, are used to scan the mouse surface for the extraction of surface geometry. The experimental acquisition time depends on how many illumination positions and how many emission wavelengths are used for imaging.

3. Methods and Materials

3.1 Phantom Fabrication

A cubic phantom ($32\times32\times29$ mm^3), composed of 1% Intralipid, 2% Agar, 20 μM bovine hemoglobin (H2625, Sigma-Aldrich Inc., St. Louis, MO), 1% sodium azide (VW3465-2, VWR, West Chester, Pennsylvania, for hemoglobin de-oxygenization), and tri-buffered saline [13], was prepared with one 12 mm capillary tube (1.5 mm outer diameter, 1.0 inner diameter) embedded inside it. The capillary tube was filled with 4.6 μM DiD (D307, Invitrogen Corporation) solution. This cubic phantom was used for the phantom experiment described in Section 4. A similar cubic phantom with two capillary tubes embedded inside it with separation of 12 mm was used for the experiment described in Section 3.3.

The cubic phantom was fabricated as follows. Water and 2% agar was heated to 95 °C and agar was dissolved. At 70 °C, saline buffer and sodium azide were added. At 60 °C, intralipid was added. The bovine hemoglobin powder was added at 50 °C. At 39.5 °C, the liquid phantom was poured into a cubic mold and kept in a refrigerator for half an hour before the phantom was taken out. The top part of the cubic phantom was cut off and the capillary tube was inserted. The cut phantom with embedded tubes was placed inside the mold. Then additional liquid phantom material was poured on the top of the cut phantom to fill the mold and complete the fabrication.

3.2 Conical Mirror Fabrication and Image Mapping

The conical mirror was made of aluminum with an outside diameter of 200 mm and length of 65 mm. Its small and large apertures are 50 and 180 mm in diameter. The imaging field of view

is 75 mm long. After the mirror was polished, silver of several micrometers thickness was coated on the conical mirror surface (Evaporated Coatings, Inc, Willow Grove, PA). The silver mirror coating has high reflectance efficiency (larger than 95%) in the NIR wavelength range.

A cube with a known surface pattern, as shown in Fig. 2a, was placed in the center of the conical mirror on a transparent stage and imaged with the EMCCD, as shown in Fig. 2b. The four arc sections separated with four red lines (added manually for clarity) are the images of the four side surfaces. The front surface of the cube also is imaged directly by the CCD camera. There is a 1:1 correspondence between a point on the surface of the cube, and the image of that point as seen by the EMCCD camera viewing the conical mirror. Since we know the true shape of the cube and the pattern on its surface, we can use the image of the cube to calibrate for the distance between the mirror and camera, the image of the central axis of the mirror in the camera plane, and the orientation of the camera relative to the mirror. We perform a least squares fit of these system parameters to a set of feature points in the image of the cube to calibrate the imaging system. The image of the cube in Fig. 2b can then be mapped back to the object coordinate space as shown in Fig. 2c.

3.3 Comparison with Flat Mirror

To compare the conical mirror measurement performance with that of multiple flat mirrors, we inserted a flat mirror directly on top of the conical mirror, keeping all other components the same as shown in Fig. 3a. A cubic phantom was placed on the platform and illuminated by a laser beam. A fluorescence image was taken, as shown in Fig. 2b. We compared the signal obtained from the top surface of the phantom as measured with the flat mirror (Fig. 2b) and the conical mirror (Fig. 2c). For the flat mirror, the image of the top surface is square in shape, whereas for the conical mirror, the image is in the shape of an arc bounded by the two black lines shown in Fig. 2c. The number of pixels in the image of the flat mirror was 5,183 containing a total of 43.8 million counts, while the conical mirror image of the top surface covered 16,499 pixels with 156.0 million counts. The ratios of the number of pixels used (the cell number in CCD) and the total camera readout values were calculated to be 3.2 and 3.6, respectively. This means that more than three times the number of photons were collected from the top surface using a conical mirror rather than a flat mirror. This same ratio would hold for a series of four flat mirrors placed around the subject compared with the conical mirror when viewing the subject from all sides. The sensitivity increment is due to the magnification effects of the conical mirror and depends on the size of imaged object. The smaller the object is, the larger the increase in collection efficiency.

3.4 Mouse Surface Extraction

For image reconstruction, the photon propagation inside phantom or mouse tissues is modeled by the diffusion equation and solved using a finite element method. For a free space (no coupling media) imaging system, the mouse surface geometry has to be obtained first. As shown in Fig. 4, all the points in the line BD share one image point D on the conical mirror. A laser line is used to scan the mouse surface, to differentiate point C from other points along the line BD and calculate its coordinates (x_C, y_C, z_C) from its image point D. The laser position is known and the equation describing the line BD can be obtained from system parameters and the coordinates of point D in the conical mirror local coordinate system. We can find the coordinates of C from

$$x_C = \frac{z_C}{H\cos\left(\frac{\pi}{2}-\gamma\right)}(H - x_B) + x_B; y_C = z_C \tan\left(\frac{\pi}{2}-\gamma\right); z_C = \frac{(x_B - x_A)\tan(\theta)}{1 - \frac{H - x_B}{H\cos\left(\frac{\pi}{2}-\gamma\right)}\tan(\theta)}$$

where γ is the radial coordinate of point D in the conical mirror local coordinate; A is the laser interception point at the central axis of the conical mirror which can be measured; θ is the laser orientation angle which can be measured. In Fig. 4, L indicates the camera position. |DE| equals H because the angle between OD and OL is 45° and DE is perpendicular to OL. B_1, C_1 and D_1 are the points corresponding to B, C and D at the different radial angle γ. Three orthogonal line lasers, which were switched on sequentially for each scanning step, were used to extract the geometry of top, left and right surfaces. The bottom surface was assumed to be a flat plane because the mouse was placed on a flat stage.

To examine the feasibility and the accuracy of the proposed surface extraction method, a rectangular object (shown in Fig. 5a) with transverse section size of 18 × 30 mm^2 was placed in the center of the conical mirror on a transparent stage. The line pattern lasers scanned the object in 50 steps, with a step size of 1 mm. The extracted geometry is plotted in Fig. 5b, where different colors indicate the surfaces extracted with different line lasers. From Fig. 5b, we see that flat surfaces could be extracted correctly although the surface images were distorted in the conical mirror image. The extracted width, the distance between the black dots and blue dots in Fig. 5b, was calculated to be 31 mm, in good agreement with the true width of 30 mm. The scattered points caused by the stage edge could be removed manually.

3.5 Finite Element Mesh Generation

The cubic phantom (Section 3.1) with known size and shape was placed in the center of the conical mirror for imaging, as shown in Fig. 6a. A cubic 3D finite element mesh with 8690 nodes and 47581 tetrahedral elements (Fig. 6b) was generated by Tetgen (Tetgen1.4.1, tetgen.berlios.de).

For the *in vivo* experiment describ**e**d in Section 4, a 26.2 g nude mouse with a xenograft tumor on its right flank was placed on the stage in the center of the conical mirror, as shown in Fig 6c. Before the fluorescence measurements were obtained, the three orthogonal line lasers scanned the mouse surface sequentially with a step size of 1 mm to extract the mouse surface geometry, as shown in Fig. 6d. The surface plots were smoothed and then used to generate a watertight surface mesh by surface reconstruction software, TIGHT COCONE (Courtesy of Professor Tamal K. Dey, Department of Computer Science and Engineering, Ohio State University) [14]. A 3D finite element mesh with 18998 nodes and 76385 tetrahedral elements was generated by Tetgen from the surface mesh, as shown in Fig. 6e.

3.6 Forward Modeling and Reconstruction algorithms

The diffusion equation in the continuous wave domain was solved using a finite element method (FEM) [15], implemented in MATLAB, at both the excitation and emission wavelengths. For n_d detector nodes, n_s point excitation sources on the animal surface, n_{em} emission wavelengths and one excitation wavelength, the system matrix was composed of the system matrix from each emission wavelength, given as

$$[A]=\begin{bmatrix} [A_1]\times C_1 \\ \vdots \\ [A_{n_{em}}]\times C_{n_{em}} \end{bmatrix} \quad (1)$$

where $[A_i]$ (i is from 1 to n_{em}) is the system matrix at i^{th} wavelength and C_i is the spectral coefficient of i^{th} wavelength obtained from Fig. 7. The dimension of submatrix $[A_i]$ is (n_d × n_S) n where n is the number of node of the finite element mesh. The submatrix is given as

$$[A_i]=\begin{bmatrix} \begin{bmatrix} \vec{\Psi}_1 \\ \vdots \\ \vec{\Psi}_{n_d} \end{bmatrix} \otimes \vec{\Phi}_1 \\ \vdots \\ \begin{bmatrix} \vec{\Psi}_1 \\ \vdots \\ \vec{\Psi}_{n_d} \end{bmatrix} \otimes \vec{\Phi}_{n_s} \end{bmatrix}, \tag{2}$$

in which $\otimes$ denotes the element product of row vectors $\vec{\Psi}_j$ and $\vec{\Phi}_k$, where j is from 1 to n_d and k is from 1 to n_s. These photon fluence vectors, defined on the finite element nodes with dimension of $1 \times n$, can be found by solving following diffusion equations in continuous wave (CW) domain,

$$\begin{aligned} -\nabla \bullet (D(\lambda_{ex})\nabla\Phi_{n_s}) + \mu_a(\lambda_{ex})\Phi_{n_s} &= S_k \\ \vec{n} \bullet (D(\lambda_{ex})\nabla\Phi_{n_s}) + b_{ex}\Phi_{n_s} &= 0 \end{aligned} \tag{3}$$

and

$$\begin{aligned} -\nabla \bullet (D(\lambda_{em})\nabla\Psi_{n_d}) + \mu_a(\lambda_{em})\Psi_{n_d} &= \Delta_j \\ \vec{n} \bullet (D(\lambda_{em})\nabla\Psi_{n_d}) + b_{em}\Phi_{n_d} &= 0. \end{aligned} \tag{4}$$

In equations (3) and (4), ∇ denotes grad operator, $\vec{n}$ is the vector normal to the boundary, b_{ex} and b_{em} are Robin boundary coefficients, the diffusion ($D(\lambda_{ex}) \cong \frac{1}{3 \bullet \mu_s'(\lambda_{ex})}, D(\lambda_{em}) \cong \frac{1}{3 \bullet \mu_s'(\lambda_{em})}$), the reduced scattering coefficients ($\mu_s'(\lambda_{ex}), \mu_s'(\lambda_{em})$) and the absorption coefficients ($\mu_a(\lambda_{ex}), \mu_a(\lambda_{em})$) are functions of the excitation wavelength λ_{ex} and emission wavelengths λ_{em}. S_k is determined by the k^{th} illumination pattern. In this study, a point illumination source is used and only the corresponding node is set to be 1 when solving Eq. (3) with finite element method. Δ_j is determined by the detector nodes. The corresponding node is set to be 1 when $\vec{\Psi}_j$ is found by solving Eq. (4) with finite element method.

With the finite element method, we obtain the linear system equation, *[A][x]=[y]*, where *[x]* is the product of the unknown fluorescence dye concentration and the quantum yield at each node to be reconstructed, and *[y]* is the measurement of light emitted from the surface of the object, obtained from the CCD images. For the Tikhonov regularization method, $F = ||[A][x] - [y]||^2 + \beta||x||^2$ is minimized to find *[x]*. A preconditioned conjugate gradient (PCG) method was used to solve the system matrix and to reconstruct the fluorescence distribution inside the phantom or the mouse body. A more detailed description of this problem formulation and iterative approaches to solving the inverse problem can be found in [16].

3.7 Optical Properties of the Phantom Materials

The absorption coefficients and the reduced scattering coefficients, at the excitation wavelength and each emission wavelength are necessary for solving Eqs. (3) and (4) for the

system matrix formulation. The optical properties at the excitation wavelength can be found with a least square algorithm, in which the square of differences between measured and calculated photon fluence was minimized [17]. Similarly, to find the optical properties at each emission wavelength, a phantom with an embedded target and known target position was illuminated with the laser beam and the square of differences between experimental and calculated fluorescence measurements was minimized. The estimated optical properties at each wavelength are listed in Table 1.

4. Results and Discussion

Fig. 7a plots the excitation and emission spectra of DiD dye [18]. To compensate for differences in filter attenuation and quantum efficiency at different wavelengths, the DiD emission spectra used in the reconstruction algorithm were measured. DiD dye solution was placed inside a transparent cuvette which was put on the imaging stage and excited with the 650 nm laser. Fig. 7b shows the measured normalized DiD emission spectra. Autofluorescence spectra from deoxygenated hemoglobin were also measured using a background phantom without target, and plotted in Fig. 7b. The nine points correspond to the nine bandpass filters installed in the filter wheel. A long pass filter was mounted in front of the filter wheel as described in Section 2. Both measurements were made from a superficial point. The absolute values of the DiD emissions are much larger than those of Hb. When the phantom was made of intralipid and agar without Hb, we did not observe any autofluorescence in the background phantom. The long pass filter was used to remove excitation photon pollution in the fluorescence measurements. However, it also attenuated the peak emission spectra from 660 to 690 nm as shown in Fig. 7 because of its wide roll off. A long pass filter with sharp edge is needed in the future.

The cubic phantom containing one capillary tube was placed in the conical mirror as shown in Fig. 6a. The 650 nm excitation laser beam scanned the front surface at 20 positions (spot size ~1 mm), as shown in Figs. 8a and 8c. Fluorescence images at wavelengths of 720, 740, 760,780, 800, 820 and 840 nm (as shown in Fig. 8b) were acquired for each illumination position. The fluorescence measurements at 1057 detector nodes on four side surfaces were determined from these images. Fig. 9a shows the conical mirror coordinate system used in the surface extraction and the local coordinate system of the cubic phantom used in the reconstruction algorithm. Fig. 9b shows the local coordinate system in the conical mirror images. The reconstructed phantom 3D images were plotted at sections with different heights. The height and coordinates of each section are shown in Figs. 9c and 9d.

Fig. 10a shows the true position of the capillary tube. Figs. 10b-f shows the reconstructed images with measurements acquired at single wavelengths of 720, 740, 760, 780 and 840 nm, respectively. These images look similar. With multispectral measurements at three wavelengths of (720, 740 and 760 nm) and (720, 780, 840 nm), the reconstructed images are plotted in Figs. 10g and 10h. In terms of target size, Fig. 10g was better than Figs. 10b–f and Fig. 10h was the best. To analyze the reconstructed images quantitatively, a profile across the target along X_L axis at Z_L=16 mm, Y_L=23 mm and along Y_L axis at Z_L=16 mm, X_L=22 mm is plotted in Figs. 11a and 11b. From Fig. 11, we see that the reconstructed target full width at half maximum (FWHM) is 3.9 mm along X_L direction and 3.5 mm along Y_L direction when measurements at three wavelengths (720, 780, 840 nm) were used. These values are 10.3 mm and 6.2 mm when one wavelength (720 nm) was used. We also see that the reconstructed target center is at X_L=22 mm and Y_L=23.2 mm for three wavelength measurements and with one wavelength measurement, the center is at X_L=21.4 mm and Y_L=21 mm. The true target center is at X_L=22 mm and Y_L=22 mm. In these studies, the regularization parameter was set to be 5.0×10^{-7}. While a thorough investigation of the resolution improvement requires that we study the noise vs. variance trade-off resulting from changes in the regularization parameter β, these

preliminary results are sufficient to indicate the potential for improvements in resolution from multispectral data. In this proof of concept experiment, the laser illumination positions are all located on the front surface. The illumination position and number could be further optimized so that image spatial resolution could be further improved and artifacts reduced. The autofluorescence from Hb was not modeled and reconstructed in this study. The larger spectral difference between DiD and Hb (see Fig. 7b) and the larger difference in optical properties (see Table 1) at 720, 780, 840 nm than at 720, 740 and 760 nm may account for why Fig. 10h has better image quality than Fig. 10g.

A 26.2 g nude mouse with a xenograft tumor (PC-3 cells, right side, dorsal, superficial, close to the bladder) was imaged with our conical mirror 3D fluorescence optical tomography imaging system 24 hours after intravenous injection of 10 nM 2DG (2DG, LI-COR, Lincoln, Nebraska). A thermocouple was used to monitor the mouse body temperature and a warm air source was switched on manually to maintain mouse body temperature close to 37 °C. A laser beam at 785 nm, with power of 50 mW and beam size of 1 mm in diameter, scanned the mouse surface at 45 locations, as shown in Fig. 12. A fluorescence image was acquired at 820 nm for each illumination position. 2334 measurements at uniformly distributed detector nodes were obtained from these fluorescence images for each illumination position. After the experiment, the mouse was euthanized immediately, frozen, sliced and imaged on a Xenogen IVIS 100 system to obtain the true fluorescence dye distribution in each section. For reconstruction, we assumed that the absorption coefficient and reduced scattering coefficient at both illumination (785 nm) and emission wavelength (820 nm) were homogeneous inside the mouse body [19]. A representative coronal section and sagittal section of the reconstructed 3D image are shown in Figs. 13a and 13b, respectively. Three transverse images crossing the tumor and bladder, the kidney and the liver are shown in Figs. 13c, 13e and 13g. The corresponding transverse cryosection images are shown in Figs. 13d, 13f and 13h. The coarse agreement between the 3D reconstructed *in vivo* data and the cryosections are encouraging in this first study.

One challenge with the conical mirror geometry is that all surfaces are viewed at once by the CCD camera and therefore the dynamic range of the camera becomes important. The EMCCD camera used in this work has a high dynamic range with a full well capacity of 37,000 electrons. In a typical whole body fluorescence measurement image of a mouse, settings are such that the EMCCD pixels immediately around the illumination spot are saturated and the SNR (signal to noise ratio) of measurements on the opposite side are calculated to be 3.6. For larger animals and/or higher absorption, a neutral density filter can be used to attenuate the light emanating from the illuminated side to improve the dynamic range.

In summary, our first phantom and *in vivo* mouse imaging results have demonstrated the potential for an efficient 3D fluorescence optical tomography system based on a conical mirror design. We have also demonstrated that a conical mirror collects emission photons more efficiently from the whole mouse than a conventional flat mirror-based imaging system. Phantom experiment results have shown that multispectral measurements can improve the spatial resolution from 6.2 mm to 3.5 mm. In the future, the effect of the number of detector nodes and finite element mesh nodes on spatial resolution will be investigated and multispectral measurements will be applied to *in vivo* mouse studies to improve the quality and resolution of these reconstructions.

Acknowledgments

This research was supported by grants from the National Institutes of Health (NIH) (R01 CA121783 and U24 CA110804). The authors thank Professor Tamal K. Dey, Department of Computer Science and Engineering, Ohio State University for providing us surface mesh generation software, and Professor Katherine W. Ferrara, Department of Biomedical Engineering, UC Davis for providing the mouse tumor model. *In vivo* imaging and cryosectioning was carried out with assistance from the UC Davis Center for Molecular and Genomic Imaging (subsidized by the UC

Davis Cancer Center Support Grant P30 CA93373). The authors thank Chris Griesemer and Jennifer Fung for technical assistance.

References and links

1. Ntziachristos V, Ripoll J, Wang LHV, Weissleder R. Looking and listening to light: the evolution of whole-body photonic imaging. Nat Biotech 2005;23:313–320.
2. Gurfinkel M, Ke S, Wen XX, Li C, Sevick-Muraca EM. Near-infrared fluorescence optical imaging and tomography. Dis Markers 2003;19:107–121. [PubMed: 15096708]
3. Chaudhari AJ, Darvas F, Bading JR, Moats RA, Conti PS, Smith DJ, Cherry SR, Leahy RM. Hyperspectral and multispectral bioluminescence optical tomography for small animal imaging. Phys Med Biol 2005;50:5421–5441. [PubMed: 16306643]
4. Zavattini G, Vecchi S, Mitchell G, Weisser U, Leahy RM, Pichler BJ, Smith DJ, Cherry SR. A hyperspectral fluorescence system for 3D in vivo optical imaging. Phys Med Biol 2006;51:2029–2043. [PubMed: 16585843]
5. Shives E, Xu Y, Jiang HB. Fluorescence lifetime tomography of turbid media based on an oxygen-sensitive dye. Opt Express 2002;10:1557–1562. [PubMed: 19461692]
6. Davis SC, Pogue BW, Springett R, Leussler C, Mazurkewitz P, Tuttle SB, Gibbs-Strauss SL, Jiang SS, Dehghani H, Paulsen KD. Magnetic resonance-coupled fluorescence tomography scanner for molecular imaging of tissue. Rev Sci Instrum 2008;79:064302. [PubMed: 18601421]
7. Graves EE, Culver JP, Ripoll J, Weissleder R, Ntziachristos V. Singular-value analysis and optimization of experimental parameters in fluorescence molecular tomography. J Opt Soc Am A 2004;21:231–241.
8. Deliolanis N, Lasser T, Hyde D, Soubret A, Ripoll J, Ntziachristos V. Free-space fluorescence molecular tomography utilizing 360 degrees geometry projections. Opt Lett 2007;32:382–384. [PubMed: 17356660]
9. Patwardhan SV, Bloch SR, Achilefu S, Culver JP. Time-dependent whole-body fluorescence tomography of probe bio-distributions in mice. Opt Express 2005;13:2564–2577. [PubMed: 19495147]
10. D'Andrea C, Spinelli L, Comelli D, Valentini G, Cubeddu R. Localization and quantification of fluorescent inclusions embedded in a turbid medium. Phys Med Biol 2005;50:2313–2327. [PubMed: 15876669]
11. Wang G, Shen H, Duraiaj K, Qian X, Cong WX. The first bioluminescence tomography system for simultaneous acquisition of multiview and multispectral Data. Int J Biom Imag 2006;8
12. Shen, H.; Cong, A.; Qian, X.; Cong, W.; Wang, G. A Cone-shaped Mirror-based 360 View Bioluminescence Tomography System. Joint Molecular Imaging Conference Abstract Book; 2007. p. 83
13. De Grand AM, Lomnes SJ, Lee DS, Pietrzykowski M, Ohnishi S, Morgan TG, Gogbashian A, Laurence RG, Frangioni JV. Tissue-like phantoms for near-infrared fluorescence imaging system assessment and the training of surgeons. J Biomed Opt 2006;11:014007. [PubMed: 16526884]
14. Dey TK, Goswami S. Tight Cocone: A Water-tight Surface Reconstructor. J Comp Inform Sci in Eng 2003;3:302–307.
15. Fedele F, Laible JP, Eppstein MJ. Coupled complex adjoint sensitivities for frequency-domain fluorescence tomography: theory and vectorized implementation. J Comput Phys 2003;187:597–619.
16. Ahn S, Chaudhari AJ, Darvas F, Bouman CA, Leahy RM. Fast iterative image reconstruction methods for fully 3D multispectral bioluminescence tomography. Phys Med Biol 2008;53:3921–3942. [PubMed: 18591735]
17. Iftimia N, Jiang HB. Quantitative optical image reconstruction of turbid media by use of direct-current measurements. Appl Opt 2000;39:5256–5261. [PubMed: 18354522]
18. Fluorescence SpectraViewer. www.invitrogen.com/site/us/en/home/support/Research-Tools/Fluorescence-SpectraViewer.html
19. Alexandrakis G, Rannou FR, Chatziioannou AF. Tomographic bioluminescence imaging by use of a combined optical-PET (OPET) system: a computer simulation feasibility study. Phys Med Biol 2005;50:4225–4241. [PubMed: 16177541]

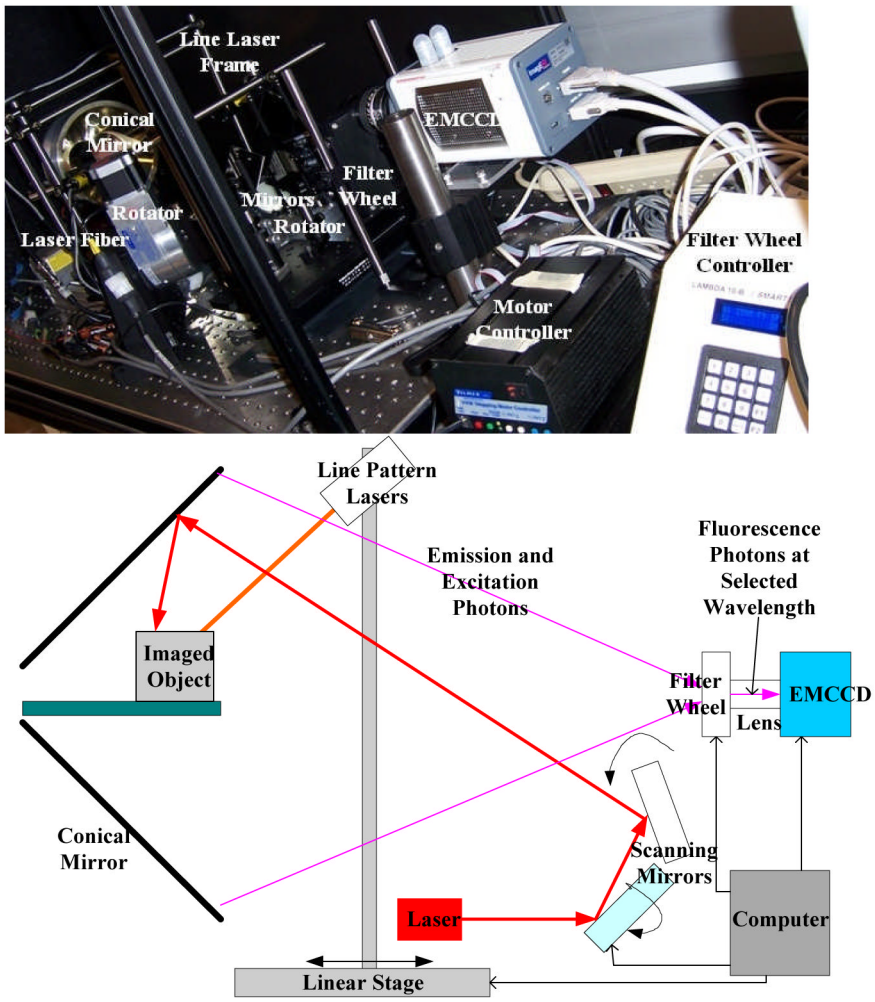

Fig. 1.

Photograph and schematic of the 3-D fluorescence optical tomography system based on a conical mirror for efficient collection of light from the entire mouse.

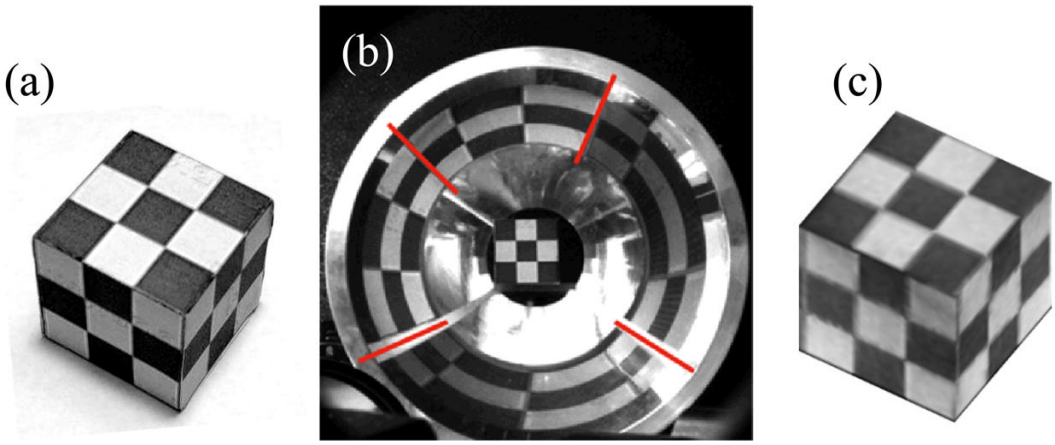

Fig. 2.
(a) A cube with known surface pattern; (b) the cube placed inside the conical mirror on a stage and imaged by the EMCCD camera; (c) the image of the cube after mapping back from the EMCCD image coordinate space to the object space.

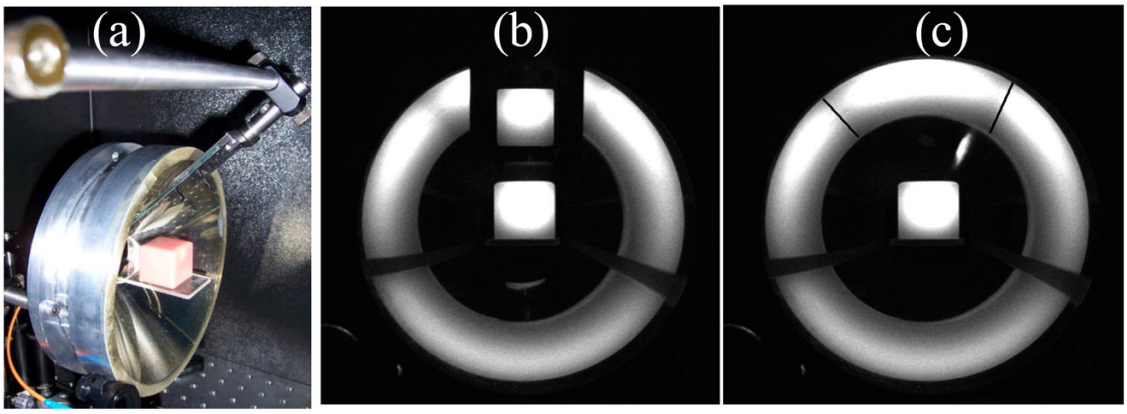

Fig. 3.

Measurement comparison between flat and conical mirrors. (a) A flat mirror was inserted inside the conical mirror; fluorescence emission photon density measurements at a wavelength of 700nm with flat mirror in place (b) and with conical mirror only (c). Note that the brightness and contrast of Figs. b and c have been adjusted to highlight the measurement region.

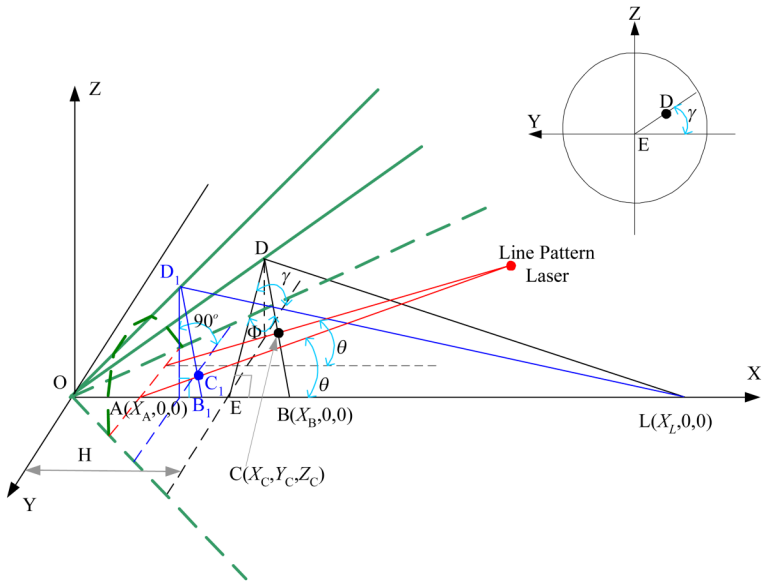

Fig. 4.

Principle of surface geometry extraction from a laser line projection on an object in a conical mirror.

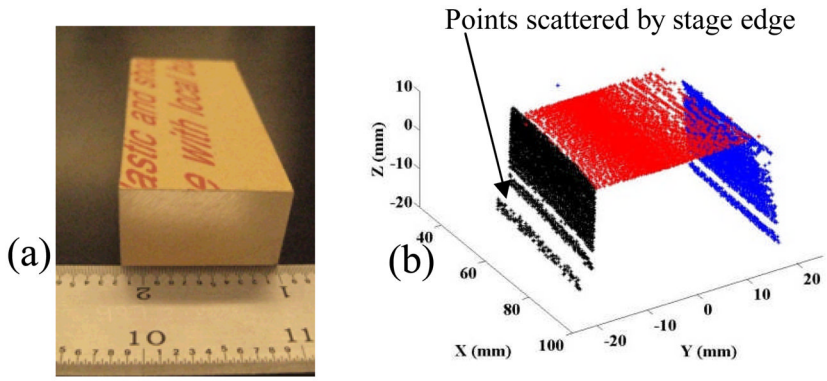

Fig. 5.
(a) A rectangular object with known size and (b) its extracted geometry.

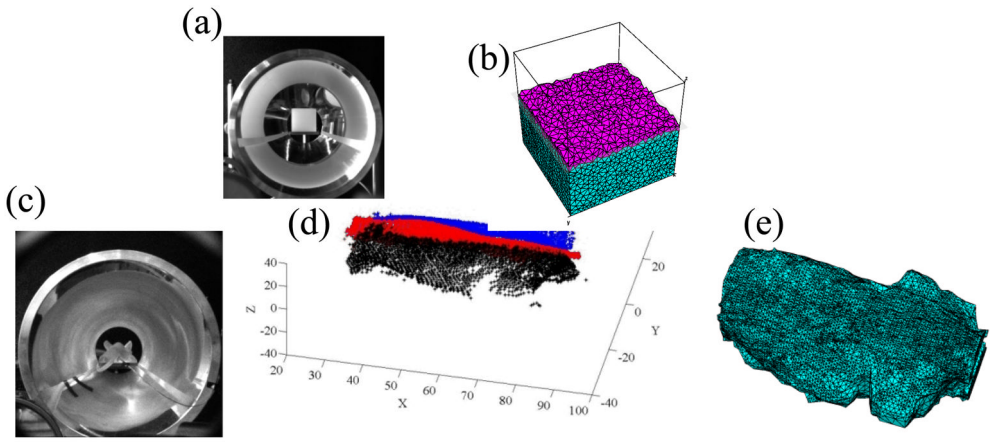

Fig. 6.

(a) photograph of the cubic phantom taken by the EMCCD camera when the phantom was placed in the conical mirror; (b) 3D mesh for cubic phantom; (c) photograph of the mouse taken by EMCCD camera when the mouse was placed in the conical mirror; (d) extracted surface plots of the mouse, where different color points were obtained from different line pattern lasers illuminating different surfaces; (e) final 3D mesh of the mouse surface geometry.

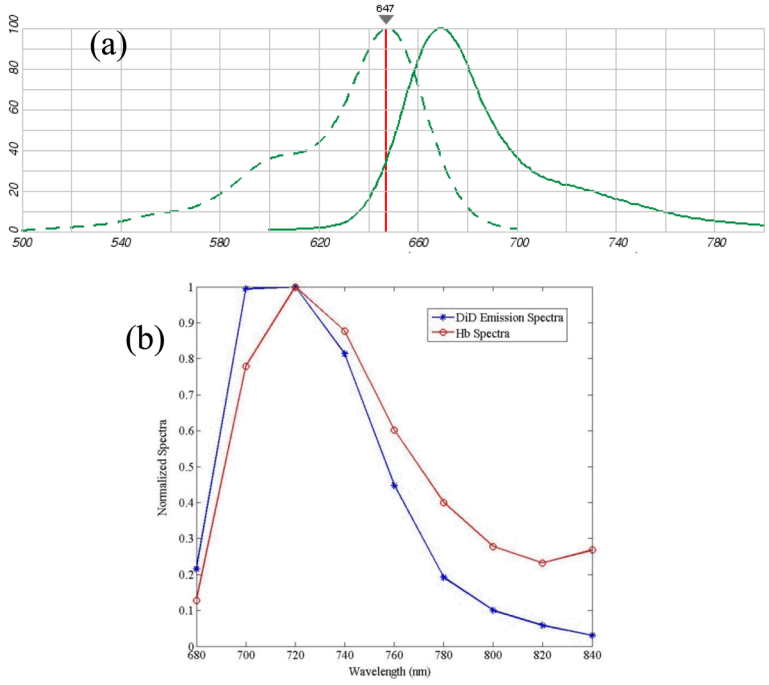

Fig. 7.

(a) The excitation (dotted line) and emission (solid line) spectra of DiD dye from Invitrogen SpectraViewer, where horizontal axis indicates the wavelength with unit nm. (b) The normalized emission spectra of DiD dye solution (blue) and deoxyhemoglobin (red) measured with the imaging system and 650 nm excitation.

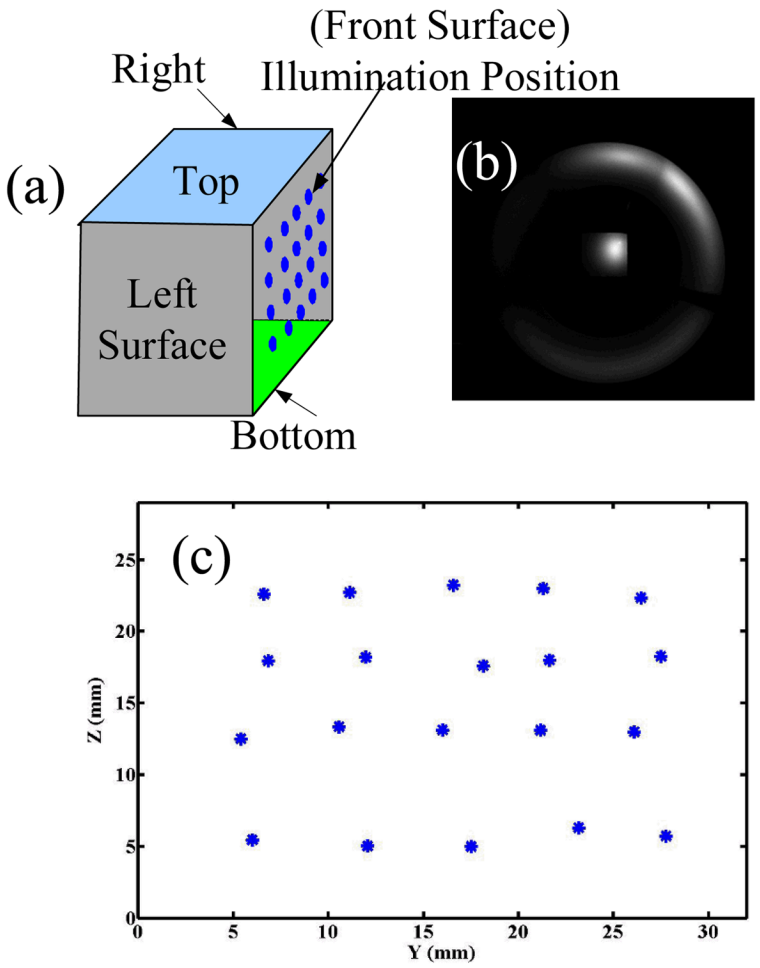

Fig. 8.

(a) Schematic of the excitation positions (blue dots) and the fluorescence measurement surfaces (left, right, top and bottom). (b) The fluorescence measurement picture taken by EMCCD for an illumination position. (c) The true illumination positions of laser beam on the front surface.

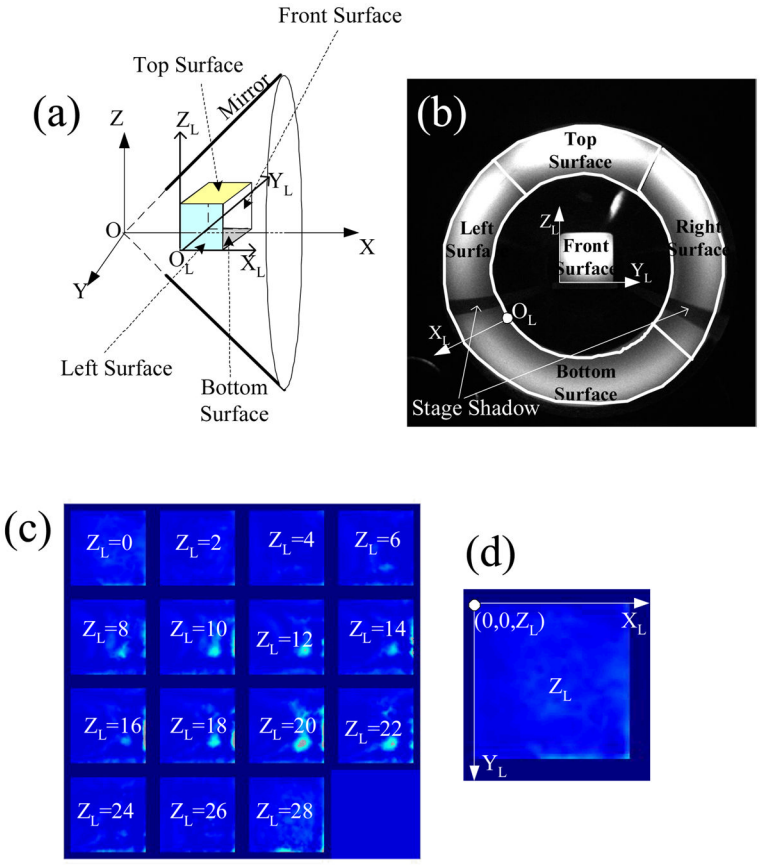

Fig. 9.

Definition of coordinate systems for phantom experiment. (a) The conical mirror coordinate system (X, Y, Z) and the local coordinate system of cubic phantom (X_L, Y_L, Z_L). (b) The local coordinate system viewed in the CCD measurement picture. (c) To view the reconstructed image in detail, the sections at different Z_L are shown. (d) The coordinates of each plotted section.

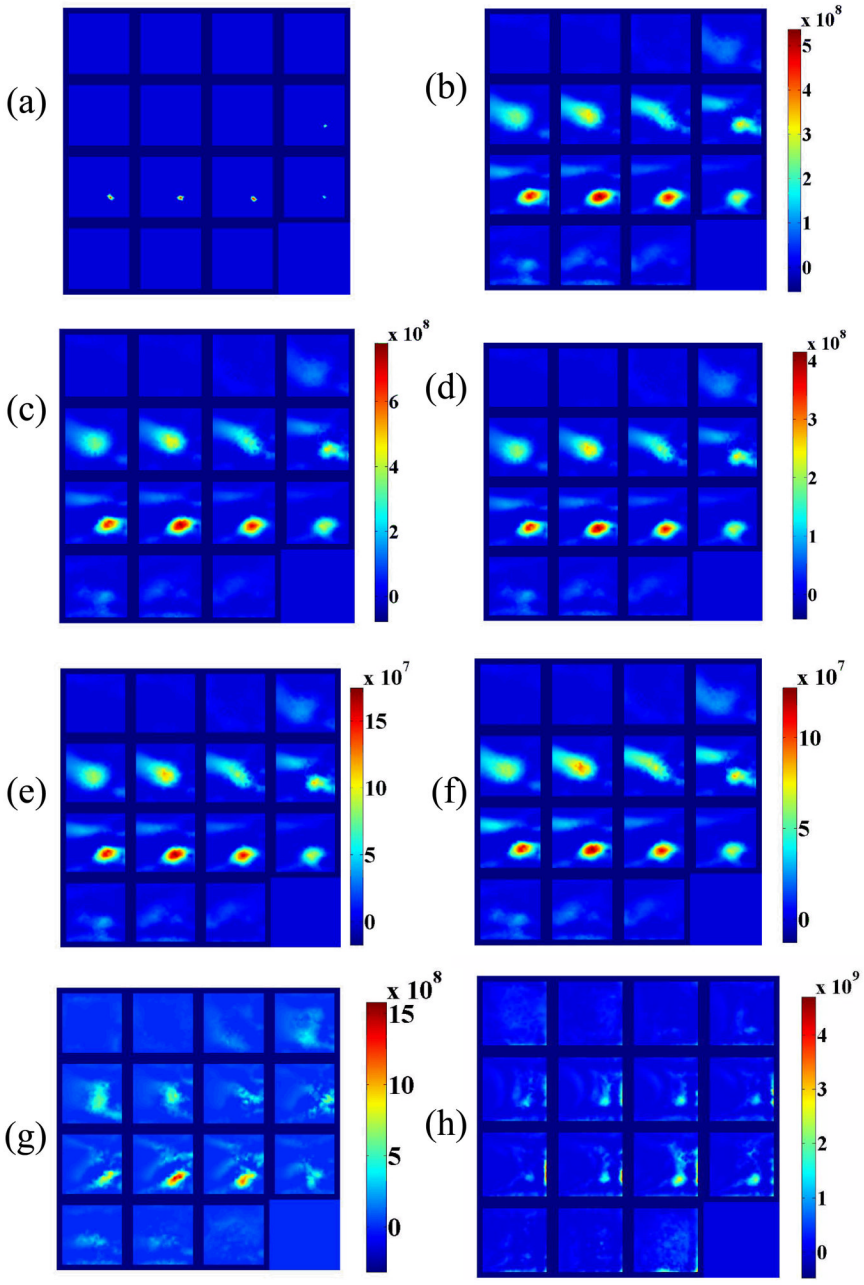

Fig. 10.

(a) True positions of the target in the cubic background. Reconstructed images with measurements at single wavelength of 720 nm (b), 740 nm (c), 760 nm (d), 780 nm (e) and 840 nm (f). (g) Reconstructed image with measurements at three wavelengths of 720 nm, 740 nm and 760 nm. (h) Reconstructed image with measurements at three wavelengths of 720 nm, 780 nm and 840 nm. Color bar indicates the concentration of fluorescence dye in arbitrary units.

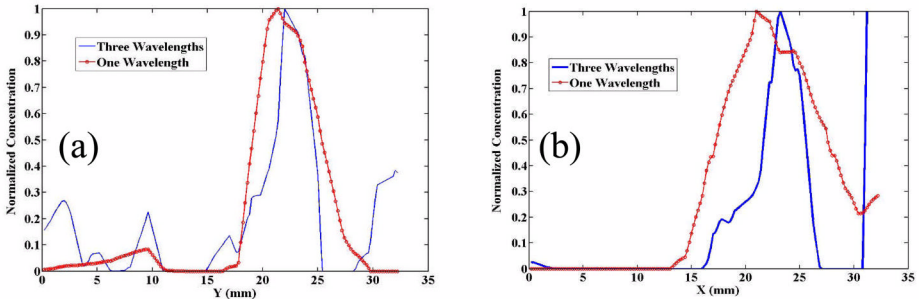

Fig. 11.

Profile plots cross the target centered at z=16 mm, y=23 mm (a) and at z=16 mm, x=22 mm (b). One wavelength was acquired at 720 nm and three wavelengths was acquired at 720, 780 and 840 nm.

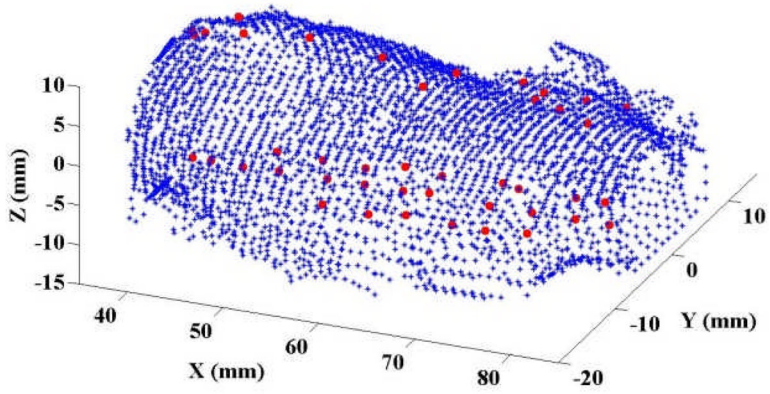

Fig. 12.

Surface plot of the mouse geometry (blue dots) and the laser illumination positions (red dots). The measurement points cover the whole body surface for each illumination position.

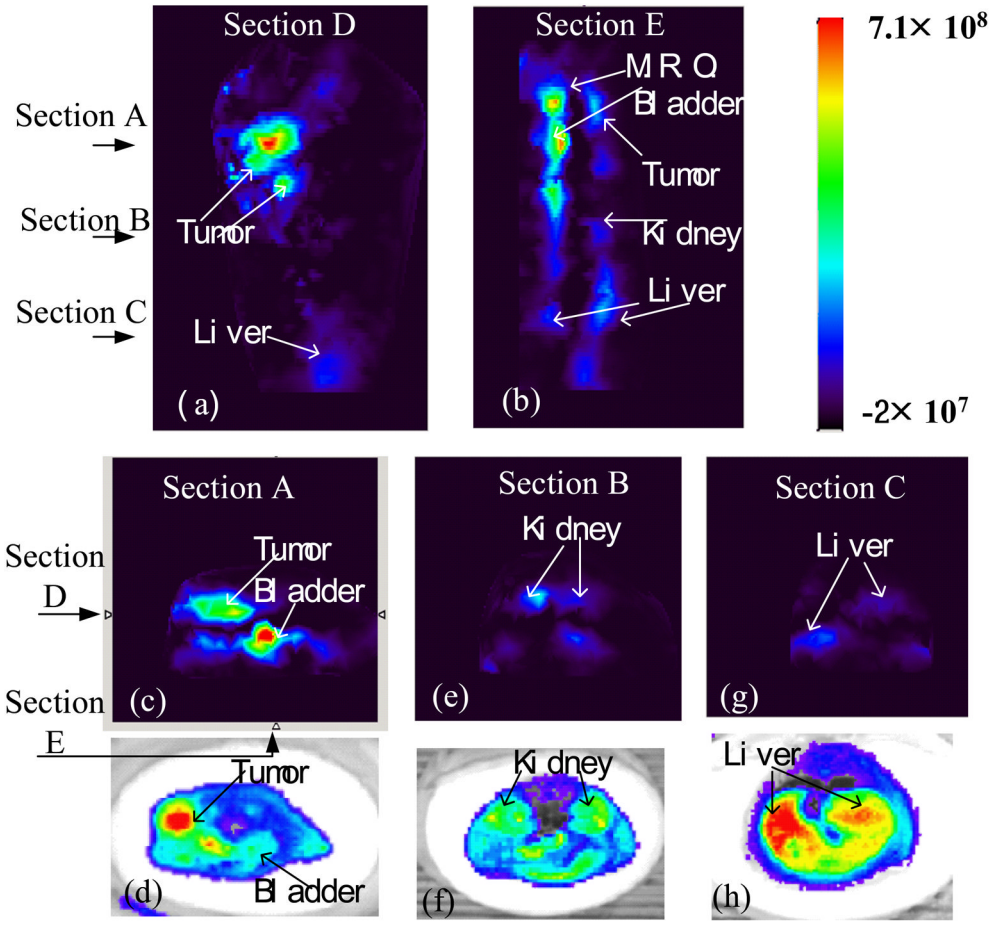

Fig. 13.

Reconstructed 3D fluorescence optical image of the mouse 24 hours after 2DG injection. (a) Coronal section; (b) sagittal section; transverse section at A cross the tumor and bladder (c), at B across the kidney (e) and at C across the liver (g); fluorescence image of mouse cryosection corresponding to section A (d), section B (f) and section C (g). MRO indicates “male reproductive organ”. The color bar indicates the reconstructed fluorescence dye concentration at arbitrary unit.

Table 1

The phantom optical properties at each wavelength

Wavelength (nm)	**650**	**680**	**700**	**720**	**740**	**760**	**780**	**800**	**820**	**840**
μ_a (mm^{-1})	0.0072	0.0126	0.0114	0.0096	0.009	0.0086	0.0074	0.0064	0.0054	0.0054
μ_s' (mm^{-1})	0.72	0.84	0.78	0.82	0.86	0.88	0.98	1.08	1.28	1.48

Opt Express. Author manuscript; available in PMC 2010 April 9.